Applied Materials Today 31 (2023) 101747

Contents lists available at ScienceDirect

Applied Materials Today

journal homepage: www.elsevier.com/locate/apmt

A physics-based machine-learning approach for modeling the temperature-dependent yield strengths of medium- or high-entropy alloys

B. Steingrimsson [a,d,*], X. Fan [b], R. Feng [c], P.K. Liaw [b]

[a] Imagars LLC, P.O. Box 261, Wilsonville, OR 97070, USA
[b] Department of Materials Science and Engineering, The University of Tennessee, Knoxville, TN, 37996, USA
[c] Neutron Scattering Division, Oak Ridge National Laboratory, Oak Ridge, TN, 37830, USA
[d] Department of Manufacturing, Mechanical and Engineering Technology, Oregon Institute of Technology, Wilsonville, OR 97070, USA

ARTICLE INFO

Keywords:
Machine learning
Medium-entropy alloy
High-entropy alloy
Temperature-dependent yield strength
High-temperature applications

ABSTRACT

Machine learning is becoming a powerful tool to accurately predict temperature-dependent yield strengths (YS) of structural materials, particularly for multi-principal-element systems. However, successful machine-learning predictions depend on the use of reasonable machine-learning models. Here, we present a comprehensive and up-to-date overview of a bilinear log model for predicting temperature-dependent YS of medium-entropy or high-entropy alloys (MEAs or HEAs). In this model, a break temperature, T_{break}, is introduced, which can guide the design of MEAs or HEAs with attractive high-temperature properties. Unlike assuming black-box structures, our model is based on the underlying physics, incorporated in the form of a priori information. A technique for the unconstrained global optimization is employed to enable the concurrent optimization of model parameters over low- and high-temperature regimes, showing that the break temperature is consistent across the YS and ultimate strength for a variety of HEA compositions. A high-level comparison between YS of MEAs/HEAs and those of Nickel-based superalloys reveals superior strength properties of selected refractory HEAs. For reliable operations, the temperature of a structural component, such as a turbine blade, made from refractory alloys, may need to stay below T_{break}. Once above T_{break}, phase transformations may start taking place, and the alloy may begin losing structural integrity.

1. Introduction

Metallic structural alloys with excellent mechanical properties, especially at elevated temperatures, remain in high demand, such as in the aerospace and nuclear industries. Unlike traditional alloys, which only contain one or two principal elements, high-entropy alloys (HEAs), also referred to as multi-principal-element alloys (MPEAs), multi-component alloys, or compositionally-complex alloys (CCAs), have been investigated extensively, since their inception in 2004 [1–8]. The carefully-designed HEAs, with either single or multiple phases, have given rise to excellent mechanical properties and vast compositional space, compared to the conventional alloys [9–26]. Studies of the Cantor alloy, CrMnFeCoNi, reveal that it can exhibit outstanding mechanical properties, particularly at cryogenic temperatures, with the ultimate tensile strength (UTS) approaching 1 GPa and the ductility of almost 100% at - 196 °C [27, 28]. Moreover, the fracture toughness is well over 200 MPa$\sqrt{\text{m}}$, and the fatigue strength is nearly 300 MPa after 10^7 cycles at room temperature [27, 29, 30].

Due to the near-infinite chemical compositional space of HEAs, finding the right chemical compositions with outstanding properties is challenging. Data analytics and machine learning (ML) can help with a rapid search of the vast compositional space, with effective tuning and optimization, and hence, expedite the development of HEAs exhibiting superior properties. It is important to keep in mind that the work on the optimization of compositions and thermomechanical treatments for HEAs has started relatively recently, and there is an enormous range of different alloy and heat-treatment options yet to be explored [27]. For background materials on ML and the motivation for the research direction proposed, on predictions of compositions yielding favorable strength properties, and on factors impacting model selection (including Occam's razor), refer to [31–33].

Further towards such an end, Bhandari et al. employed a ML method based on a regression technique of random forest (RF) to predict the yield strengths (YS) of HEAs at a desired temperature [34]. The yield

---

* Corresponding author.
E-mail addresses: baldur@imagars.com, baldur.steingrimsson@oit.edu (B. Steingrimsson).

https://doi.org/10.1016/j.apmt.2023.101747
Received 5 August 2022; Received in revised form 28 December 2022; Accepted 20 January 2023
Available online 1 February 2023
2352-9407/© 2023 Elsevier Ltd. All rights reserved.

strengths of MoNbTaTiW and HfMoNbTaTiZr were predicted at 800 °C and 1,200 °C, using a RF model. The authors determined that the results were consistent with experiments and concluded that the RF regression model predicted the YS of HEAs at the desired temperatures with high accuracy [34]. Wen et al. presented a relationship characterizing solid-solution strengthening (SSS) for HEAs in terms of electronegativity difference of the constituent elements [35]. The authors introduced a ML model, which exhibits superior performance in predicting SSS / hardness of HEAs, compared to existing physics-based models. The ML model involves the feature construction and selection, which is configured such as to capture the salient descriptors [35]. Note that the RF-prediction model of [34] and the feature construction and selection of [35] can be considered pure (or black-box) ML models, at least for the most parts, in the sense that the underlying physics are not built directly into the models. The authors of [35] proposed the following formula for SSS in HEAs:

$$\Delta\sigma_{SS} = \xi\ Z\ G\ \delta X_r, \tag{1}$$

where Z represents a fitting parameter, ξ a structure factor consistent with a T model [36], G the shear modulus of the HEAs, and δX_r an electronegativity mismatch between elements. This formula, however, differs significantly from established, analytical models for SSS. According to Kozar et al. [37], the solid-solution hardening in Nickel-base superalloys can be modeled as

$$\Delta\sigma_{ss} = \sum_i \left(\frac{d\sigma}{\sqrt{dC_i}} \sqrt{C_i} \right), \tag{2}$$

where C_i represents the concentration of the ith alloying element, but $d\sigma / \sqrt{dC_i}$ is a strengthening coefficient that reflects the strengthening potency of the alloying element, i. For further information, refer to the exposition of the work of Kozar et al. in the supplementary manuscript [37]. The structure of Eq. (2) differs significantly from that of Eq. (1). Hence, the outcomes of the two models may also differ considerably.

Zhang et al. modeled the effect of temperature on the tensile behavior of an interstitial HEA, with the nominal composition of Fe49.5Mn30Co10Cr10C0.5 (atomic percent, at.%), in [38], but focused on the development of a micro-mechanism-based crystal-plasticity model (a multi-scale model), as opposed to ML. Note that while the model of [38] is physics-based, it is not a ML model. Qi et al. present in [39] a phenomenological method, where the binary-phase diagrams are analyzed to predict phase properties of HEAs. The authors introduced several phase-diagram-inspired parameters and employed ML to classify 600+ reported HEAs based on these parameters. For a further review of ML and high-throughput studies on high-entropy materials (HEMs), refer to [40] and the references listed therein.

In terms of important contributions (novelty), this study presents a bilinear log model for accurately predicting the yield strengths of MEAs and HEAs across temperature. This model consists of separate exponentials, for a low-temperature and a high-temperature regime, with a break temperature, T_{break}, in between. The bilinear log model accounts for the underlying physics, in particular, diffusion processes that are required to initiate phase transformations in the high-temperature regime [41]. Furthermore, we show in Ref. [32] how a piecewise linear regression can be employed to extend the model beyond two exponentials and yield accurate fit, in case of a non-convex objective function caused by hump(s) in the data. Earlier models for the temperature dependence of yield strengths (YS) only accounted for a single exponential [42, 43]. Therefore, there was no break temperature, T_{break}. We consider the break point particularly important for the optimization of the high-temperature properties of alloys. For reliable operations, the temperature of turbine blades or disks made from refractory alloys may need to stay below T_{break}. Once the alloy temperature exceeds T_{break}, the alloy can lose its strength rapidly due to rapid diffusion, leading to the easy dislocation motion and dissolution of strengthening phases [41]. We consider T_{break} a fundamental parameter for the design of alloys with attractive high-temperature properties, one warranting the inclusion in the alloy specifications. Hence, it is important to be able to accurately estimate T_{break}, e.g., using the global optimization approach presented in [32].

In terms of impact, this study addresses a physics-based, i.e., not a black box, approach to ML and data analytics. Such approaches may be preferred in materials science, first because they involve fewer parameters than the black-box models, and hence, require fewer input data for the accurate parameter estimation. With experiments often being time-consuming and expensive, in the case of materials science, high-quality input data tend to be a scarce resource. Secondly, the physics-based approaches to ML help establish causal links between output observations and the behavior of the underlying material system.

2. Results

2.1. Database and categorization of MEA and HEA compositions

The database described in [31–33] comprises the base for this study. New additions include data from [44–52]. The authors made a concerted effort to conduct a systematic study of the HEA literature and make the analysis as comprehensive and up to date as possible. Extending the work of [53], we define medium-entropy alloy (MEA) or HEA compositions with 3d-transition metals only as of Type 1, compositions comprising of transition metals with large atomic-radius elements (such as Al/Ti/V/Mo) as of Type 2, compositions comprising of refractory elements of Type 3 and other compositions as of Type 4 (such as precious-element-containing HEAs and hexagonal-close-packed-structured HEAs). As Fig. 1 illustrates, we have generalized the categorization from [53] such as to accommodate MEA compositions, defined as compositions comprised of three (3) principal elements, in addition to the HEA compositions[1]. Not accounting for separate configurations of the same composition, we analyzed three (3) distinct MEA or HEA compositions of Type 1, ten (10) of Type 2, ninety-nine (99) of Type 3, and none (0) of Type 4.

2.2. Bilinear log model applied to analysis of yield strengths for MEAs and HEAs

To identify compositions with potential in retaining strengths at elevated temperatures, we summarize the reported MEAs and HEAs, according to the classifications in Fig. 1, in the Supplementary Tabs. S1 – S3, Fig. 2, as well as Figs. S2 – S125 of the Supplementary Manuscript. Fig. 2 and S2 – S125 of the Supplementary Manuscript provide graphical insight into the superiority of the bilinear model, as estimated, using the mean squared error (MSE), defined as

$$MSE = \frac{1}{N} \sum_{i=1}^{N} \left(YS_{model,}(T_i) - YS_{meas,}(T_i) \right)^2, \tag{3}$$

over a model based on a single exponential. Here $YS_{model,}(T_i)$ represents the modeled yield strength at a temperature T_i, $YS_{meas,}(T_i)$ denotes the measured yield strength at the temperature T_i, and N represents the overall number of measured yield strength values in the data set for the alloy under study. For a given alloy, the bilinear log model can similarly be compared to the single-exponential model on the basis of $\sqrt{MSE}$ or $\log(MSE)$. Supplementary Tabs. S1 – S2 quantify the comparison with the single-exponential model in detail. Consistent with [32], the results were derived, using the same global optimization approach, applied separately to individual alloys, to obtain a tighter fit and more accurate estimation of T_{break}, than for separate optimization over the low and high-temperature regimes. Note that for most of the MEA and HEA

---

[1] Senkov et al. refer to MEAs and HEAs collectively as complex concentrated alloys (CCAs) [41].

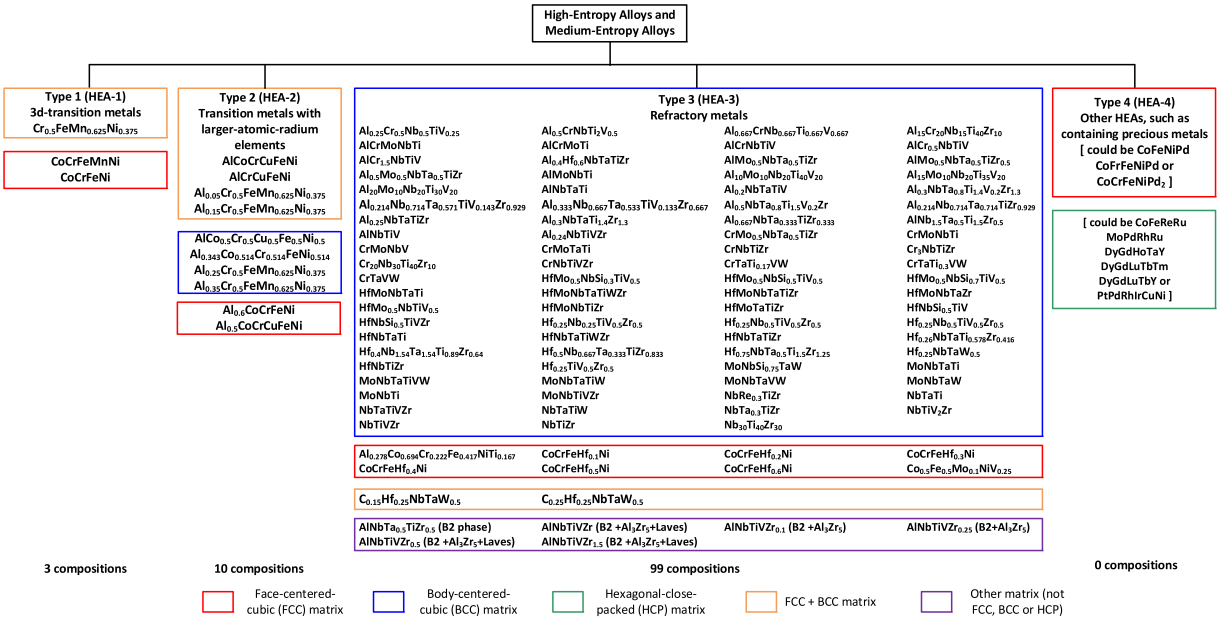

Fig. 1. Classification of high-entropy alloys and medium-entropy alloys. The figure comprises an adapted version of Fig. 1 from [53], now generalized such as to also include MEAs. Secondary phases, such as intermetallic phases, have been omitted for simplicity.

compositions, the solvus temperatures were estimated, using the rule of mixing, i.e., as the weighted mean of the melting temperatures of the constituent elements, employing the same weight percentages as in the compositions [32].

2.3. *Comparison of break temperatures for YS vs. Ultimate Strength (US) for MEAs and HEAs*

Figs. 3–5 and Supplementary Figs. S126 - S135 summarize the comparison of the break temperatures for YS vs. US for the MEAs and HEAs. Here we have separately fitted the bilinear log model to a set of experimentally measured data points for the yield strength, represented by the red circles in Fig. 3, and the ultimate strength, represented by the black circles in Fig. 3. Aside from the composition of MoNbTaVW (the single outlier in Fig. 5), the break temperatures for the YS and the US seem quite similar. In the case of MoNbTaVW, and as the Supplementary Fig. S132(a) illustrates, the disparity seems to be caused by a single data point for the US at $T = 1{,}200$ °C and may highlight the need for data curation [33].

2.4. *Comparison of yield strengths for MEAs and HEAs vs. superalloys*

Fig. 6 summarizes the comparison of the yield strengths for the MEAs and HEAs vs. the superalloys. The HEA compositions of $C_{0.25}Hf_{0.25}NbTaW_{0.5}$, $MoNbSi_{0.75}TaW_{0.5}$, and MoNbTaVW seem to exhibit the most graceful degradation of YS (the smallest slope) at high temperatures. But the compositions of $MoNbSi_{0.75}TaW$, CrTaVW, and $AlMo_{0.5}NbTa_{0.5}TiZr$ tend to yield the highest strength for the lower-temperature regime.

3. Discussion

The FCC + BCC composition of $C_{0.25}Hf_{0.25}NbTaW_{0.5}$ [50], the BCC + silicide composition $MoNbSi_{0.75}TaW$ [54], the BCC + Laves composition CrTaVW [55], and the BCC composition MoNbTaVW [41, 56] seem to offer favorable strength at elevated temperatures (above 800 °C), according to Fig. 6, whereas the BCC + silicide composition of $MoNbSi_{0.75}TaW$ [54], the BCC + Laves composition of CrTaVW [55], and the BCC + B2 composition of $AlMo_{0.5}NbTa_{0.5}TiZr$ [41] exhibit attractive strength properties at lower temperatures (25 °C – 800 °C). While CrTaVW and $MoNbSi_{0.75}TaW$ appear to exhibit the best performance for the low-temperature and high-temperature regimes. Note that we are basing this observation on only three (3) data points, in case of CrTaVW, and four (4) data points, in case of $MoNbSi_{0.75}TaW$.

As explained in [32], we expect the bilinear log model (two exponentials) to suffice for most refractory HEAs (HEA-3). As noted in [57], the mechanisms of microscopic slips (dislocation slips) can lead to the pronounced temperature dependence of mechanical strengths. It is unlikely that cross slip from {111} to (100), such as the one producing an anomalous yield stress phenomenon in CMSX-4, single-crystal, nickel-based superalloys (a hump between the low-temperature and high-temperature regimes, necessitating a tri-linear log model) will happen in refractory HEAs [32].

The loss of strengths in single-phase refractory BCC HEAs is related to the activation of the diffusion-controlled deformation mechanism, which typically occurs at $T \geq 0.5$ - $0.6\ T_m$ [41]. The rapid decrease in strengths of multi-phase refractory HEAs, with increasing temperatures above 1,000 °C, is, on the other hand, partially caused by the dissolution of secondary phases [41]. Further, Feng et al. highlight three alloy properties leading to superior high-temperature strengths, namely (1) large atomic-size and elastic-modulus mismatches, (2) insensitive temperature-dependence of elastic properties, and (3) the dominance of non-screw character dislocations [58].

3.1. *More on the comparison between break temperatures for YS vs. US*

The consistency of the break temperature across YS and US and across the HEA compositions looks very comforting. The consistency lends credence to the bilinear log model and suggests that the break temperature is indeed a universal parameter. The coefficient of determination, R^2, in Fig. 5 consolidates the comparison into a single parameter. In case of Fig. 4, ‘Yield Strength (1)’ and ‘Yield Strength (2)’ represent YS values corresponding to two separate fabrication runs, post-processing conditions, or possibly microstructures. For example, in the case of AlCrMoNbTi, Refs. [41] and [59] reported multi-phase BCC + Laves (almost single-phase) microstructures for samples annealed for 20 hr. at 1,300 °C, whereas Ref. [57] found similar YS for almost single-phase BCC microstructures for samples annealed for 20 hr. at 1, 300 °C. In the case of MoNbTaVW and the disparity between the break temperature for the YS and US in Fig. 5 and the Supplementary

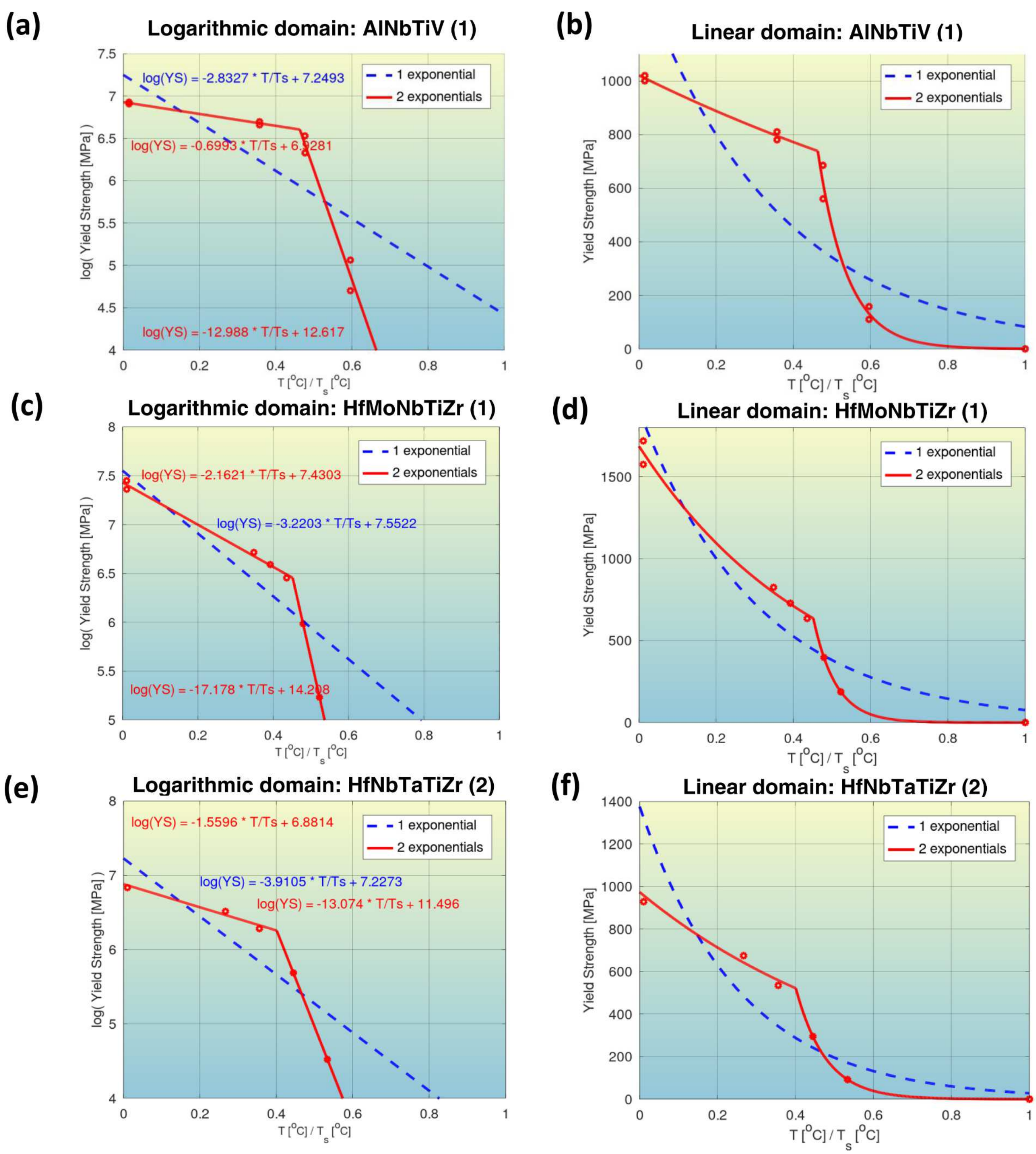

Fig. 2. Quantification of modeling accuracy of the bilinear log model and comparison to that of a model with a single exponential. Top row: Composition No. 42 from Supplementary Table S1 (AlNbTiV, BCC phase). Middle row: Composition No. 87 from Supplementary Table S2 (HfMoNbTiZr, BCC phase). Bottom row: Composition No. 98 from Supplementary Table S3 [HfNbTaTiZr (2), BCC phase]. The red, hollow markers represent yield strength values experimentally measured at the temperature values indicated.

Fig. S132, it is worth noting that the YS of 735 MPa and the US of 943 MPa at T = 1,200 °C were both reported by [56]. It appears that measurement errors may need to be accounted for here, first in the estimation of the YS and US and then in the assessment of the associated break temperatures. The authors noted: “Further increases in temperature to 1,400°C and 1,600°C led to a rapid decline in the yield stress and apparent softening” [56].

3.2. More on the need for a tri-linear log model

We noticed in Fig. 6 as well as in Supplementary Figs. S4, S27, S69, S70, and S71 that the compositions of $Al_{0.5}$CoCrCuFeNi, AlMoNbTi, CrMoNbTi, CrMoNbV, and CrMoTaTi exhibited a relatively flat behavior in an intermediate temperature regime, in contrast to the two linear regimes. Although these cases differ from the hump reported in [32], corresponding to the anomalous yield-strength phenomenon, these cases may still necessitate a tri-linear log model.

Reference [57] offers an explanation for this type of tri-linear behavior for intrinsic temperature-dependent yield strengths in BCC metals and substitutional solid solutions:

1 At the low temperatures, plastic deformation of the BCC metals and alloys is believed to be mediated by the thermally-activated formation and movement of kink pairs [57].

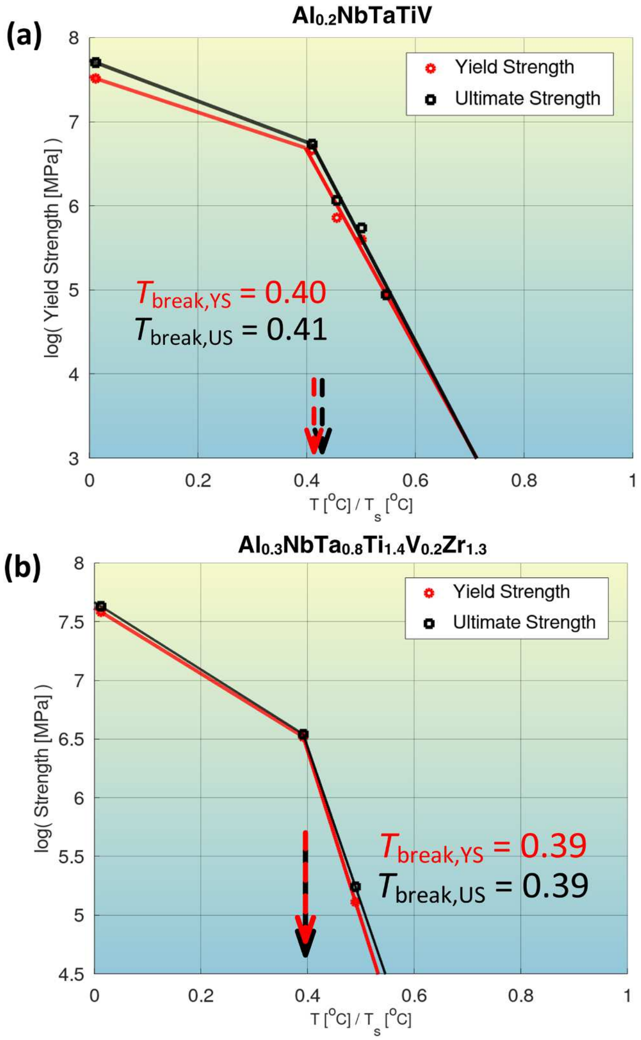

Fig. 3. Comparison between break temperatures for the yield strength and ultimate strength of the compositions, $Al_{0.2}NbTaTiV$ (above) and $Al_{0.3}NbTa_{0.8}Ti_{1.4}V_{0.2}Zr_{1.3}$ (below). For a similar comparison for the other compositions listed in Fig. 4, refer to Supplementary Figs. S124 – S133.

2 Above certain "critical temperature," a strength plateau is reached, where the strength becomes virtually strain-rate independent [57].
3 When exceeding the temperature of approx. 0.4 T_m, diffusional processes can lead to a rapid decrease of the yield stress, and the YS comes strain-rate dependent again [57].

In the case of the tri-linear model, we are looking at two break temperatures, T_{break1} and T_{break2} [32]. But [57] only references one such temperature and refers to it as "critical temperature" or "knee temperature". This seemingly corresponds to T_{break1} in our model.

3.3. Further high-level comparison of yield strengths for MEAs and HEAs vs. superalloys

The motivation for this study of the strengths of MEAs and HEAs is to accelerate the search for high-strength structural materials at high temperatures, for applications in thermal-protection systems and/or gas-turbine engines. The compositions of $MoNbSi_{0.75}TaW$ and CrTaVW seem to exhibit the best performance (highest YS), according to Fig. 6, for the low-temperature and high-temperature regimes. The appearance of Fig. 6 is affected in part by the fact that we are interpolating straight line segments between a limited number of data points for any given composition.

Out of the 124 MEA and HEA configurations, whose yield strengths that we analyzed, only 10 were conducted under tension but 114 under compression. Specifically, the yield strength measurements for $C_{0.25}Hf_{0.25}NbTaW_{0.5}$, $MoNbSi_{0.75}TaW$, CrTaVW, MoNbTaVW, and $AlMo_{0.5}NbTa_{0.5}TiZr$ were all conducted under compression. Similarly, out of the 36 superalloy compositions whose yield strengths that we analyzed, the vast majority was conducted under tension in accordance with standards, such as the American Society for Testing and Materials (ASTM) E-8 [60]. Specifically, the yield-strength measurements for Inconel 718, Haynes 230, and Rene 95 were all conducted under tension. It is well known that the tension test is much more difficult than the compression test, since the test samples may need to be machined into dog bone shapes and polished to comply with standards, such as ASTM E-8 [60]. One runs the risk of introducing defects, during polishing, and deteriorating the mechanical properties. However, according to Supplementary Table 2 of [32], the ultimate strength under tension usually appears to be a little bit smaller than under compression (up to $\sim$ 100 MPa). The difference between the strengths of the refractory HEAs and the superalloys in Fig. 6, on the other hand, ranges from 100 – 2,000+ MPa (in other words, much exceeds what can be explained in terms of the difference between tension and compression tests). Note, furthermore, the superalloys satisfy a broad range of additional requirements for high-temperature structural applications, including tensile ductility, fracture toughness, oxidation resistance, creep strength, fatigue strength, and processability [17].

It is important to note that Fig. 6 exhibits significant similarity and consistency with Fig. 20 of [17], esp. as far as superior temperature-dependent strength properties of $AlMo_{0.5}NbTa_{0.5}TiZr$ and MoNbTaVW relative to the superalloys (e.g., Inconel 718 or Haynes 230) are concerned. Inconel 718 [(Al,Nb,Ti)5Co1Cr21Fe19Mo2Ni52] is a precipitation-strengthened alloy used widely in the gas-turbine industry for rotating disks, but Haynes 230 (Co4Cr27Fe3Mo1Ni60W5) is a solid-solution (SS)-strengthened alloy used for static sheet parts [17]. As shown in Fig. 6, both Inconel 718 and Haynes 230 superalloys exhibit an obvious softening behavior above ~800°C, which is also a common issue for conventional superalloys. Therefore, refractory HEAs show greater potential in obtaining high operating temperatures toward and near the melting temperatures of Ni-based superalloys.

As reflected in Fig. 6, most refractory HEAs outperform Haynes 230, and some show potential to extend the use temperature of blades and disks beyond current superalloys. The noticeable drop in YS for MoNbTaVW in Fig. 6 at $T \geq 1{,}600^{\circ}C$ is consistent with the rapid decrease at $T \geq 0.6\, T_m$ [56]. The rule of mixture estimates the melting temperature of MoNbTaVW as 2,724 °C.

3.4. Conclusions and future research

In conclusion, we proposed a bilinear log model for predicting the YS of MEAs and HEAs across temperatures and studied its effectiveness for 112 distinct compositions (124 configurations). We considered the break temperature, T_{break}, an important parameter for the design of materials with favorable high-temperature properties, one warranting inclusion in alloy specifications. For reliable operation, and not accounting for coatings, the operating temperature for the corresponding alloys may need to stay below T_{break}. Those refractory HEAs with high T_{break} values can be used to guide the selection of proper chemical compositions for designing advanced refractory HEAs. For example, the elements used in HfMoNbTaTi, $Hf_{0.25}NbTaW_{0.5}$, MoNbTaVW, and NbTaTiW refractory HEAs with T_{break} values at or above 1,200 ^{o}C (Table S2) can help the design of high-performance refractory HEAs, in which the constituent elements can be properly selected based on these four refractory model alloys. Earlier models for the temperature dependence of the yield strength only accounted for a single exponential. Thus, there was no break temperature.

We showed that the break temperature was consistent across YS and US and across a number of HEA compositions. This trend suggested that

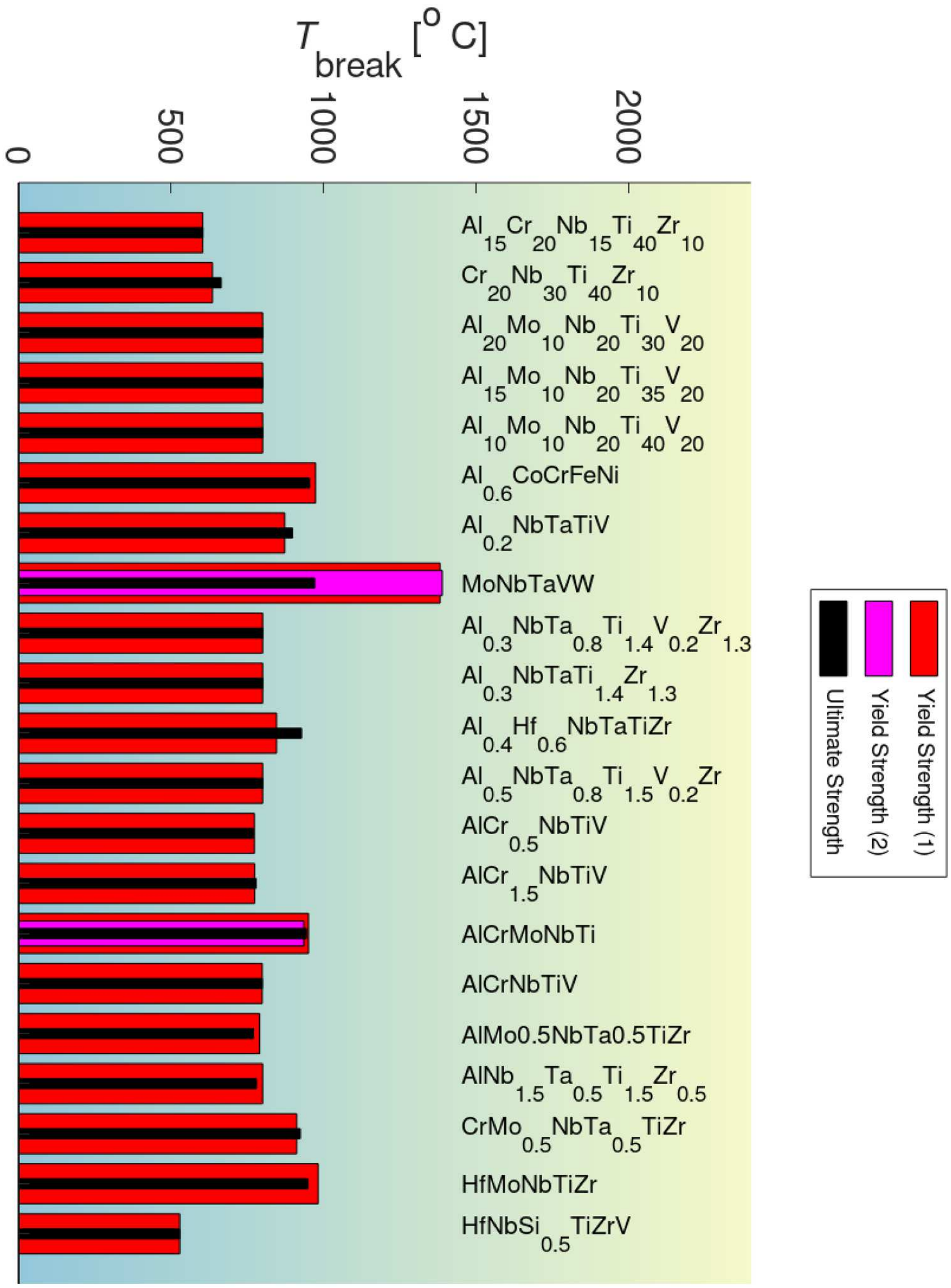

Fig. 4. Further comparison of T_{break} derived from the YS to those derived from the US [32].

the break temperature was indeed a universal parameter, and hence, lent credence to our model. We, further, noticed that the compositions AlMoNbTi, CrMoNbTi, CrMoTaTi, and CrMoNbV exhibited a relatively-flat behavior in an intermediate temperature regime, in contrast to the two linear regimes, possibly necessitating a tri-linear log model. To elucidate these observations, we drew upon explanations from [57] regarding intrinsic temperature-dependent yield strengths in BCC metals and substitutional solid solutions. Finally, our observations regarding the superior strength behavior of refractory HEAs (the category HEA-3), compared to Ni-based superalloys, were consistent with those of Miracle et al. [17], Senkov et al. [41], and Diao et al. [53]. With a caveat for the limited number of data points available, it appeared the compositions of $MoNbSi_{0.75}TaW$ and CrTaVW exhibited the best performance for the low-temperature (25 °C – 800 °C) and the high-temperature (above 800 °C) regimes.

Future research may involve (1) measurements of yield strengths of the YS of MEAs and HEAs under tension, (2) identifications of additional MEA or HEA compositions exhibiting high YS both in the low and high-temperature regimes, or (3) identifications of MEA or HEA compositions exhibiting favorable balance of properties, in particular between the strength and ductility (high tensile ductility).

4. Methods

While the primary emphasis here is on the yield strength, the optimization of the mechanical properties is assumed to reside within a framework for joint optimization [32].

4.1. *Methodology for maximization of the YS*

Our approach entails accurately capturing the input sources that contribute to variations in the YS observed (to variations in the output).

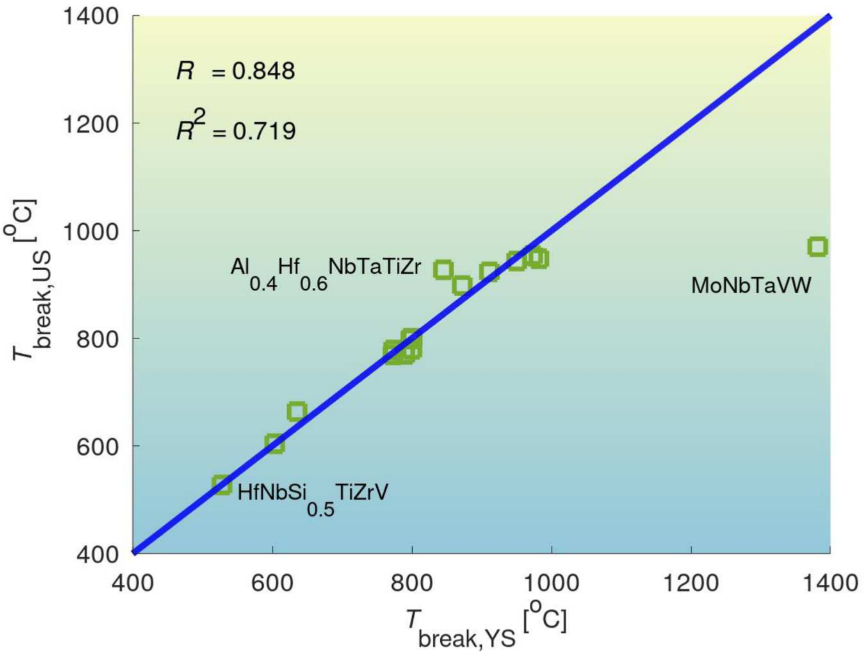

Fig. 5. Correlation of T_{break} derived from the YS with T_{break} derived from the US [32].

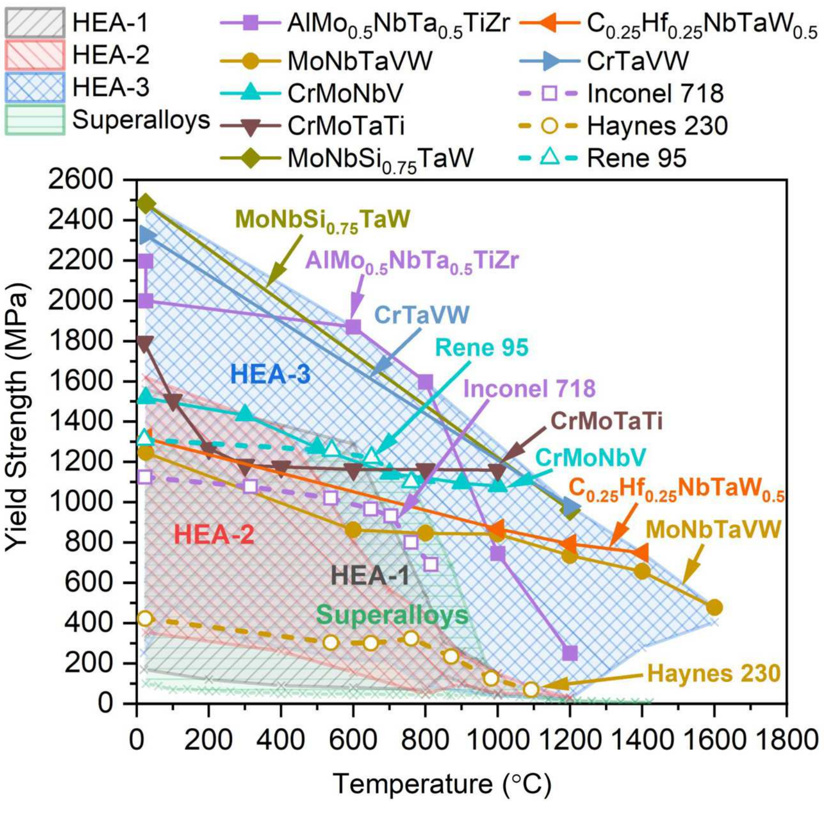

Fig. 6. Comparison of MEAs and HEAs yielding the best performance, in terms of temperature-dependent yield strengths, with superalloys yielding the best performance (based on the dataset from Supplementary Table S1 – Supplementary Table S3 as well as Fig. 2 of [53]).

We presently model the input combination as [32]

$$\text{Input} = (\text{composition},\ T,\ \text{process},\ \text{defects},\ \text{grain size},\ \text{microstructure}) \tag{4}$$

“Defects” are here defined broadly such as to include inhomogeneities, impurities, dislocations, or unwanted features. “T” denotes temperature. Similarly, the term, “microstructure,” broadly represents microstructures, at a nano or micro scale, as well as phase properties, and the term “process” broadly refers to the manufacturing process and post-processing. Correspondingly, the term, “grain size,” generally refers to the distribution in grain sizes. Section 4.4 of [33] allows for dependence between input sources, and Section 4.5 of [33] outlines the expected dependence of the alloy strength on the individual input sources listed. We summarize the prediction model as [32]

$$\begin{aligned}\mathrm{YS} \;=\; & h[\mathrm{composition},\ T,\ \mathrm{process},\ \mathrm{defects(process},T),\\ & \mathrm{grains(process},T),\ \mathrm{microstructure\ (process},T)]\end{aligned} \tag{5}$$

4.2. Methodology for modeling YS at elevated temperatures

Inspired by Figs. 3(c) and 3(d) of [32], together with physics-based insights from [41], we model the temperature dependence of the YS (*T*), in terms of a bilinear log model, parametrized by the melting temperature, T_m, as follows:

$$YS(T) = min(log(YS_1(T)), log(YS_2(T))), \tag{6}$$

$$YS_1(T) = exp(-C_1 * T / T_m + C_2), \qquad 0 < T < T_{break}, \tag{7}$$

$$YS_2(T) = exp(-C_3 * T / T_m + C_4), \qquad T_{break} < T < T_m. \tag{8}$$

There is a separate physics (diffusion)-induced constraint on T_break [41]:

$$0.35 \lesssim T_\mathrm{break} \Big/ T_\mathrm{m} \lesssim 0.55, \tag{9}$$

and a continuity constraint between the low-temperature and the high-temperature regimes:

$$YS_1(T_{break}) = YS_2(T_{break}); \tag{10}$$

$$T_\mathrm{break} = \frac{(C_4 - C_2)}{(C_3 - C_1)} T_\mathrm{m}. \tag{11}$$

As explained in [32], a conceptually-simple approach for fitting the model in Eqs. (6) – (11) to the YS data available consists of first deriving the constant coefficients, C_1 and C_2, by applying linear regression to data points available to the lowest temperature region ($0 < T < 0.35\ T_\mathrm{m}$) as well as to the intermediate region ($0.35\ T_\mathrm{m} \leq T \leq 0.55\ T_\mathrm{m}$). One may then derive the constants, C_3 and C_4, by applying linear regression to data points available to the intermediate ($0.35\ T_\mathrm{m} \leq T \leq 0.55\ T_\mathrm{m}$) and high-temperature ($T > 0.55\ T_\mathrm{m}$) regions. Note that T_break does not need to be known beforehand. Supported by Eq. (11), T_break is an inherent property of a given alloy that comes out of the model as the break point between the two linear regions. The model in Eqs. (6) – (8) consists of only four (4) independent parameters, C_1, C_2, C_3, and C_4, which simply can be estimated by applying linear regression separately to low-temperature and high-temperature regimes, even to a fairly small data set. Note, moreover, that for a new alloy system, T_m, does not need to be known experimentally in advance either; a rough estimate for T_m can be obtained, using "the rule of mixing" and a more refined estimate obtained, employing Calculation of Phase Diagram (CALPHAD) simulations [33].

A superior approach for deriving the coefficients, C_1, C_2, C_3, and C_4, entails concurrent optimization over the low-temperature and high-temperature regimes using the global optimization. Here, one seeks to minimize

$$\underset{C_1,C_2,C_3,C_4}{min}\ \underset{i}{\mathrm{norm}_2}\left((YS(T_i) - y_i)^2\right), \tag{12}$$

where y_i represents the YS values measured,

$$YS(T_i) = min(log(YS_1(T_i)), log(YS_2(T_i))), \tag{13}$$

and $\mathrm{US}_1(T_i)$ and $\mathrm{US}_2(T_i)$ are modeled, using Eqs. (7) and (8), respectively. Matlab offers a function, fminunc(), for solving this type of unconstrained minimization over a generic function. The function fminunc () utilizes a quasi-Newton method by default, to minimize over the unconstrained function, but can also employ a trust-region approach. For the purpose of saving memory, the trust-region algorithm allows the user to provide a Hessian multiply function, i.e., a function yielding the result of a Hessian-times-vector product, without computing the Hessian directly. Both in the case of the quasi-Newton method and the trust-region approach, the user is required to provide an initial solution estimate, for the global minimization.

Depending on the grain sizes and compositions comprising the alloys, a tri-linear log model may yield a better fit for certain alloys [28, 32]:

$$YS(T) = min(YS_1(T), YS_2(T), YS_3(T)), \tag{14}$$

$$YS_1(T) = exp(-C_1 * T / T_m + C_2), \qquad 0 < T < T_{break1}, \tag{15}$$

$$YS_2(T) = exp(-C_3 * T / T_m + C_4), \qquad T_{break1} < T < T_{break2}, \tag{16}$$

$$YS_3(T) = exp(-C_5 * T / T_m + C_6), \qquad T_{break2} < T < T_m \tag{17}$$

Code availability

Matlab comprises the software package primarily used for this study. Supplementary Figs. S7 and S8 of [32] contain a Matlab source code for the objective functions optimized in case of the bilinear or trilinear log model, respectively.

Author contributions

B.S. and P.K.L conceived the project. B.S. performed the modeling of the temperature-dependent yield strength and put together the supplementary manuscript. X.F. helped prepare the database and carefully reviewed the manuscript for comparison with previously published work [32]. R.F. contributed towards analytical modeling. All authors edited and proofread the final manuscript and participated in discussions.

CRediT authorship contribution statement

B. Steingrimsson: Conceptualization, Methodology, Software, Writing – original draft. **X. Fan:** Writing – review & editing. **R. Feng:** Investigation, Writing – review & editing. **P.K. Liaw:** Conceptualization, Writing – review & editing.

Declaration of Competing Interest

The authors declare no competing interests (financial or non-financial).

Data availability

The data in this paper, including those in the Supplementary Figures, can be requested by contacting the corresponding author

Acknowledgements

XF and PKL very much appreciate the support of the U.S. Army Research Office Project (W911NF-13-1-0438 and W911NF-19-2-0049) with the program managers, Drs. M. P. Bakas, S. N. Mathaudhu, and D. M. Stepp. RF and PKL thank the support from the National Science Foundation (DMR-1611180, 1809640, and 2226508) with the program directors, Drs. J. Madison, J. Yang, G. Shiflet, and D. Farkas. XF and PKL also appreciate the support from the Bunch Fellowship. XF and PKL would like to acknowledge funding from the State of Tennessee and Tennessee Higher Education Commission (THEC) through their support of the Center for Materials Processing (CMP). BS very much appreciates the support from the National Science Foundation (IIP-1447395 and IIP-1632408), with the program directors, Drs. G. Larsen and R. Mehta, from the U.S. Air Force (FA864921P0754), with J. Evans as the program manager, and from the U.S. Navy (N6833521C0420), with Drs. D. Shifler and J. Wolk as the program managers.

The authors also want to thank Dr. Liang Jiang for introducing them to some of the background literature on analytical modeling of the yield strength.

Supplementary materials

Supplementary material associated with this article can be found, in the online version, at doi:10.1016/j.apmt.2023.101747.

References

[1] B. Cantor, I.T.H. Chang, P. Knight, A.J.B. Vincent, Microstructural development in equiatomic multicomponent alloys, Mater. Sci. Eng. R. Rep. A (375) (2004) 213–218.

[2] J.W. Yeh, S.K. Chen, S.J. Lin, J.Y. Gan, T.S. Chin, T.T. Shun, C.H. Tsau, S.Y. Chang, Nanostructured high entropy alloys with multiple principal elements: novel alloy design concepts and outcomes, Adv. Eng. Mater. 6 (2004) 299–303.

[3] E.P. George, D. Raabe, R.O. Ritchie, High-entropy alloys, Nat. Rev. Mater. 4 (2019) 515–534.

[4] P. Shi, R. Li, Y.L. Wen, Y. Zhong, W. Ren, Z. Shen, T. Zheng, J. Peng, X. Liang, P. Hu, N. Min, Y. Zhang, Y. Ren, P.K. Liaw, D. Raabe, Y.D. Wang, Hierarchical crack buffering triples ductility in eutectic herringbone high-entropy alloys, Science 374 (6565) (2021) 912–918.

[5] M.C. Gao, J.-W. Yeh, P.K. Liaw, Y. Zhang, High Entropy Alloys - Fundamentals and Applications, Springer, 2016.

[6] Z. Li, S. Zhao, R.O. Ritchie, M.A. Meyers, Mechanical properties of high-entropy alloys with emphasis on face-centered cubic alloys, Progr. Mater. Sci. 102 (2019) 296–345.

[7] Y. Zhang, T.T. Zuo, Z. Tang, M.C. Gao, K.A. Dahmen, P.K. Liaw, Z.P. Lu, Microstructures and properties of high-entropy alloys, Progr. Mater. Sci. 61 (2014) 1–93.

[8] Y.F. Ye, Q. Wang, J. Lu, C.T. Liu, Y. Yang, High-entropy alloy: challenges and prospects, Mater. Today 19 (6) (2016) 349–362.

[9] J. Moon, E. Tabachnikova, S. Shumilin, T. Hryhorova, Y. Estrin, J. Brechtl, P. K. Liaw, W. Wang, K.A. Dahmen, A. Zargaran, J.W. Bae, H.S. Do, B.J. Lee, H.S. Kim, Deformation behavior of a Co-Cr-Fe-Ni-Mo medium-entropy alloy at extremely low temperatures, Mater. Today 50 (2021) 55–68.

[10] X. Feng, J.U. Surjadi, R. Fan, X. Li, W. Zhou, S. Zhao, Y. Lu, Microalloyed medium-entropy alloy (MEA) composite nanolattices with ultrahigh toughness and cyclability, Mater. Todays 42 (2021) 10–16.

[11] Q. Ding, X. Fu, D. Chen, H. Bei, B. Gludovatz, J. Li, Z. Zhang, E.P. George, Q. Yu, T. Zhu, R.O. Ritchie, Real-time nanoscale observation of deformation mechanisms in CrCoNi-based medium-to high-entropy alloys at cryogenic temperatures, Mater. Today 25 (2019) 21–27.

[12] P. Shi, Y. Zhong, Y. Li, W. Ren, T. Zheng, Z. Shen, B. Yang, J. Peng, P. Hu, Y. Zhang, P.K. Liaw, Y. Zhu, Multistage work hardening assisted by multi-type twinning in ultrafine-grained heterostructural eutectic high-entropy alloys, Mater. Today 41 (2020) 62–71.

[13] H. Luo, W. Lu, X. Fang, D. Ponge, Z. Li, D. Raabe, Beating hydrogen with its own weapon: Nano-twin gradients enhance embrittlement resistance of a high-entropy alloy, Mater. Today 21 (10) (2018) 1003–1009.

[14] Y. Bu, Y. Wu, Z. Lei, X. Yuan, H. Wu, X. Feng, J. Liu, J. Ding, Y. Lu, H. Wang, Z. Lu, W. Yang, Local chemical fluctuation mediated ductility in body-centered-cubic high-entropy alloys, Mater. Today 46 (2021) 28–34.

[15] P. Wang, Y. Bu, J. Liu, Q. Li, H. Wang, W. Yang, Atomic deformation mechanism and interface toughening in metastable high entropy alloy, Mater. Today 37 (2020) 64–73.

[16] V. Chaudhary, R. Chaudhary, R. Banerjee, R.V. Ramanujan, Accelerated and conventional development of magnetic high entropy alloys, Mater. Today 49 (2021) 231–252.

[17] O.N. Senkov, D.B. Miracle, A critical review of high entropy alloys and related concepts, Acta Mater. 122 (2017) 448–511.

[18] Q. Pan, L. Zhang, R. Feng, Q. Lu, K. An, A.C. Chuang, J.D. Poplawsky, P.K. Liaw, L. Lu, Gradient cell-structured high-entropy alloys with exceptional strength and ductility, Science 374 (6570) (2021) 984–989.

[19] W. Li, D. Xie, D. Li, Y. Zhang, Y. Gao, P.K. Liaw, Mechanical behavior of high-entropy alloys, Prog. Mater Sci. 118 (100777) (2021) 1–142.

[20] Q. Ding, Y. Zhang, X. Chen, X. Fu, D. Chen, S. Chen, L. Gu, F. Wei, H. Bei, Y. Gao, Tuning element distribution, structure and properties by composition in high-entropy alloys, Nature 574 (7777) (2019) 223–227.

[21] Z. Lei, X. Liu, Y. Wu, H. Wang, S. Jiang, S. Wang, X. Hui, Y. Wu, B. Gault, P. Kontis, D. Raabe, L. Gu, Q. Zhang, H. Chen, H. Wang, J. Liu, K. An, Q. Zeng, T.G. Nieh, Z. Lu, Enhanced strength and ductility in a high-entropy alloy via ordered oxygen complexes, Nature 563 (7732) (2018) 546–550.

[22] Z. Li, K.G. Pradeep, Y. Deng, D. Raabe, C.C. Tasan, Metastable high-entropy dual-phase alloys overcome the strength-ductility trade-off, Nature 534 (7606) (2016) 227–230.

[23] F. Wang, G.H. Balbus, S. Xu, Y. Su, J. Shin, P.F. Rottmann, K.E. Knipling, J. C. Stinville, L.H. Mills, O.N. Senkov, Multiplicity of dislocation pathways in a refractory multiprincipal element alloy, Science 370 (6512) (2020) 95–101.

[24] T. Yang, Y. Zhao, Y. Tong, Z. Jiao, J. Wei, J. Cai, X. Han, D. Chen, A. Hu, J. Kai, Multicomponent intermetallic nanoparticles and superb mechanical behaviors of complex alloys, Science 362 (6417) (2018) 933–937.

[25] S. Wei, S.J. Kim, J. Kang, Y. Zhang, Y. Zhang, T. Furuhara, E.S. Park, C.C. Tasan, Natural-mixing guided design of refractory high-entropy alloys with as-cast tensile ductility, Nat. Mater. 19 (2020) 1175–1181.

[26] R. Zhang, S. Zhao, J. Ding, Y. Chong, T. Jia, C. Ophus, M. Asta, R.O. Ritchie, A. M. Minor, Short-range order and its impact on the CrCoNi medium-entropy alloy, Nature 581 (7808) (2020) 283–287.

[27] B. Cantor, A personal perspective on the discovery and Significance of multicomponent high-entropy alloys, in: J. Brechtl, P.K. Liaw (Eds.), High-Entropy Materials: Theory, Experiments, and Applications, Springer Nature, Switzerland AG, 2021, pp. 1–36.

[28] F. Otto, A. Dlouhý, C. Somsen, H. Bei, G. Eggeler, E.P. George, The influence of temperature and microstructure on the tensile properties of a CoCrFeNiMn high-entropy alloy, Acta Mater. 61 (2013) 5743–5755.

[29] B. Gludovatz, A. Hohenwarter, D. Catoor, E.H. Chang, E.P. George, R.O. Ritchie, A fracture resistant high-entropy alloy for cryogenic applications, Science 345 (2014) 1153–1158.

[30] Y.Z. Tian, S.J. Sun, H.R. Lin, Z.F. Zhang, Fatigue behavior of CoCrFeMnNi high-entropy alloy under fully reversed cyclic deformation, J. Mater. Sci. Technol. 35 (2019) 334–340.

[31] B. Steingrimsson, X. Fan, A. Kulkarni, D. Kim, P.K. Liaw, Machine Learning to Accelerate Alloy Design, 5 February 2020. USA Patent 16/782,829.

[32] B. Steingrimsson, X. Fan, X. Yang, M.C. Gao, Y. Zhang, P.K. Liaw, Predicting temperature-dependent ultimate strengths of body-centered cubic (BCC) high-entropy alloys, npj Comput. Mater. 7 (152) (September 24, 2021) 1–10.

[33] B. Steingrimsson, X. Fan, A. Kulkarni, M.C. Gao, P.K. Liaw, Machine learning and data analytics for design and manufacturing of high-entropy materials exhibiting mechanical or fatigue properties of interest, in: James Brechtl, Peter K. Liaw (Eds.), High-Entropy Materials: Theory, Experiments, and Applications, Springer Nature, Switzerland AG, 2021, pp. 115–238.

[34] U. Bhandari, M.R. Rafi, C. Zhang, S. Yang, Yield strength prediction of high-entropy alloys using machine learning, Mater. Today Commun. 26 (101871) (2021).

[35] C. Wen, C. Wang, Y. Zhang, S. Antonov, D. Xue, T. Lookman, Y. Su, Modeling solid solution strengthening in high entropy alloys using machine learning, Acta Mater. 212 (116917) (2021).

[36] I. Toda-Caraballo, P.E.J. Rivera-Díaz-del-Castillo, Modelling solid solution hardening in high entropy alloys, Acta Mater. 85 (2015) 14–23.

[37] R.W. Kozar, A. Suzuki, W.W. Milligan, J.J. Schirra, M.F. Savage, T.M. Pollock, Strengthening Mechanisms in Polycrystalline Multimodal Nickel-Base Superalloys, Metall. Mater. Trans. A 40 (2009) 1588–1603.

[38] X Zhang, X Lu, J Zhao, Q Kan, Z Li, G Kang, Temperature effect on tensile behavior of an interstitial high entropy alloy: Crystal plasticity modeling, Int. J. Plast. 150 (103201) (March 2022).

[39] J. Qi, A.M. Cheung, S.J. Poon, High entropy alloys mined from binary phase diagrams, Sci. Rep. 9 (15501) (2019).

[40] E.W. Huang, W.J. Lee, S.S. Singh, P. Kumar, C.Y. Lee, T.N. Lam, H.H. Chin, B. H. Lin, P.K. Liaw, Machine-learning and high-throughput studies for high-entropy materials, Mater. Sci. Eng. R. 147 (100645) (January 2022).

[41] O.N. Senkov, S. Gorsse, D.B. Miracle, High temperature strength of refractory complex concentrated alloys, Acta Mater. 175 (2019) 394–405.

[42] Z. Wu, H. Bei, G.M. Pharr, E.P. George, Temperature dependence of the mechanical properties of equiatomic solid solution alloys with face-centered cubic crystal structures, Acta Mater. 81 (2014) 428–441.

[43] F. Maresca, W.A. Curtin, Mechanistic origin of high strength in refractory BCC high entropy alloys up to 1900K, Acta Mater. 182 (2020) 235–249.

[44] C.K.H. Borg, C. Frey, J. Moh, T.M. Pollock, S. Gorsse, D.B. Miracle, O.N. Senkov, B. Meredig, J.E. Saal, Expanded dataset of mechanical properties and observed phases of multi-principal element alloys, Sci. Data 7 (430) (2020).

[45] Q. Li, T.W. Zhang, J.W. Qiao, S.G. Ma, D. Zhao, P. Lu, Z.H. Wang, Mechanical properties and deformation behavior of dual-phase Al0. 6CoCrFeNi high-entropy alloys with heterogeneous structure at room and cryogenic temperatures, J. Alloys Compd. 816 (152663) (2020).

[46] T. Cao, L. Ma, L. Wang, J. Zhou, Y. Wang, B. Wang, Y. Xue, High temperature deformation behavior of dual-phase Al0.6CoCrFeNi high-entropy alloys, J. Alloys Compd. 836 (155305) (2020).

[47] Z.Q. Xu, Z.L. Ma, M. Wang, Y.W. Chen, Y.D. Tan, X.W. Cheng, Design of novel low-density refractory high entropy alloys for high-temperature applications, Mater. Sci. Eng. A 755 (2019) 318–322.

[48] N. Yurchenko, E. Panina, S. Zherebtsov, N. Stepanov, Design and characterization of eutectic refractory high entropy alloys, Materialia 16 (101057) (2021).

[49] X. Li, W. Guo, B. Liu, A. Fu, J. Li, Q. Fang, Y. Liu, Microstructure and mechanical properties of TaNbVTiAlx refractory high-entropy alloys, Entropy 22 (3) (2020) 282.

[50] S. Wu, D. Qiao, H. Zhang, J. Miao, H. Zhao, J. Wang, Y. Lu, T. Wang, T. Li, Microstructure and mechanical properties of CxHf0. 25NbTaW0. 5 refractory high-entropy alloys at room and high temperatures, J. Mater. Sci. 97 (2022) 229–238.

[51] H. Yi, Y. Zhang, R. Xie, M. Bi, D. Wei, High-temperature deformation behaviors of the C-Doped and N-doped high entropy alloys, Metals 11 (10) (2021) 1517.

[52] Z.Q. Xu, Z.L. Ma, G.H. Xia, M. Wang, T.B. Xie, X.W. Cheng, Microstructures and mechanical properties of CoCrFeNiHfx high-entropy alloys, Mater. Sci. Eng. A Struct. Mater. 792 (2020), 139820.

[53] H.Y. Diao, R. Feng, K.A. Dahmen, P.K. Liaw, Fundamental deformation behavior in high-entropy alloys: an overview, Curr. Opin. Solid State Mater. Sci. 21 (5) (2017) 252–266.

[54] Z. Guo, A. Zhang, J. Han, J. Meng, Correction to: Effect of Si additions on microstructure and mechanical properties of refractory NbTaWMo high-entropy alloys, J. Mater. Sci. 54 (13) (2019).

[55] O.A. Waseem, J. Lee, H.M. Lee, H.J. Ryu, The effect of Ti on the sintering and mechanical properties of refractory high-entropy alloy TixWTaVCr fabricated via spark plasma sintering for fusion plasma-facing materials, Mater. Chem. Phys. 210 (2018) 87–94.

[56] O.N. Senkov, G.B. Wilks, J.M. Scott, D.B. Miracle, Mechanical properties of Nb25Mo25Ta25W25 and V20Nb20Mo20Ta20W20 refractory high entropy alloys, Intermetallics 19 (2011) 698–706.

[57] H. Chen, A. Kauffmann, S. Laube, I.C. Choi, R. Schwaiger, Y. Huang, K. Lichtenberg, F. Muller, B. Gorr, H.J. Christ, M. Heilmaier, Contribution of lattice distortion to solid solution strengthening in a series of refractory high entropy alloys, Metall. Mater. Trans. A 49 (2018) 772–781.

[58] R. Feng, B. Feng, M.C. Gao, C. Zhang, J.C. Neuefeind, J.D. Poplawsky, Y. Ren, K. An, M. Widom and P.K. Liaw, "Superior high-temperature strength in a supersaturated refractory high-entropy alloy," Adv. Mater., vol. 33, no. 48, 2021.

[59] H. Chen, A. Kauffmann, B. Gorr, D. Schliephake, C. Seemuller, J.N. Wagner, H. J. Christ, M. Hailmaier, Microstructure and mechanical properties at elevated temperatures of a new Al-containing refractory high-entropy alloy Nb-Mo-Cr-Ti-Al, J. Alloys Compd. 661 (2016) 206–215.

[60] ASTM International, Standard Test Methods for Tension Testing of Metallic Materials (Designation: E8/E8M - 13a), 2013, 100 Barr Harbor Drive, PO Box C700, West Conshohocken PA 19428-2959 USA.